Methods for In-Flight Wing Shape Predictions of Highly Flexible Unmanned Aerial Vehicles: Formulation of Ko Displacement Theory

William L. Ko and Van Tran Fleischer
NASA Dryden Flight Research Center
Edwards, California

August 2010

NASA STI Program…in Profile

Since its founding, NASA has been dedicated to the advancement of aeronautics and space science. The NASA scientific and technical information (STI) program plays a key part in helping NASA maintain this important role.

The NASA STI program operates under the auspices of the Agency Chief Information Officer. It collects, organizes, provides for archiving, and disseminates NASA's STI. The NASA STI program provides access to the NASA Aeronautics and Space Database and its public interface, the NASA Technical Report Server, thus providing one of the largest collections of aeronautical and space science STI in the world. Results are published in both non-NASA channels and by NASA in the NASA STI Report Series, which includes the following report types:

- TECHNICAL PUBLICATION. Reports of completed research or a major significant phase of research that present the results of NASA Programs and include extensive data or theoretical analysis. Includes compilations of significant scientific and technical data and information deemed to be of continuing reference value. NASA counterpart of peer-reviewed formal professional papers but has less stringent limitations on manuscript length and extent of graphic presentations.

- TECHNICAL MEMORANDUM. Scientific and technical findings that are preliminary or of specialized interest, e.g., quick release reports, working papers, and bibliographies that contain minimal annotation. Does not contain extensive analysis.

- CONTRACTOR REPORT. Scientific and technical findings by NASA-sponsored contractors and grantees.

- CONFERENCE PUBLICATION. Collected papers from scientific and technical conferences, symposia, seminars, or other meetings sponsored or co-sponsored by NASA.

- SPECIAL PUBLICATION. Scientific, technical, or historical information from NASA programs, projects, and missions, often concerned with subjects having substantial public interest.

- TECHNICAL TRANSLATION. English-language translations of foreign scientific and technical material pertinent to NASA's mission.

Specialized services also include organizing and publishing research results, distributing specialized research announcements and feeds, providing help desk and personal search support, and enabling data exchange services.

For more information about the NASA STI program, see the following:

- Access the NASA STI program home page at *http://www.sti.nasa.gov*

- E-mail your question via the Internet to help@sti.nasa.gov

- Fax your question to the NASA STI Help Desk at 443-757-5803

- Phone the NASA STI Help Desk at 443-757-5802

- Write to:
  NASA STI Help Desk
  NASA Center for AeroSpace Information
  7115 Standard Drive
  Hanover, MD 21076-1320
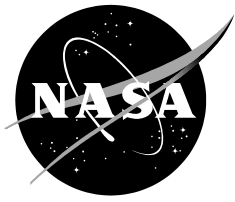
Methods for In-Flight Wing Shape Predictions of Highly Flexible Unmanned Aerial Vehicles: Formulation of Ko Displacement Theory

William L. Ko and Van Tran Fleischer
NASA Dryden Flight Research Center
Edwards, California

August 2010

The structural shape prediction method described in this report is protected under U.S. Patent No. 7,520,176, issued April 21, 2009. Therefore, those interested in using the method should contact the NASA Innovative Partnership Program Office at the Dryden Flight Research Center for more information.

ABSTRACT

Displacement equations are developed for a cantilever tubular wing spar under bending, torsion, and combined bending and torsion loading. The displacement equations are expressed in terms of strains measured at multiple sensing stations equally spaced on the surface of the wing spar. The bending and distortion strain data can then be input to the displacement equations to calculate slopes, deflections, and cross-sectional twist angles of the wing spar at the strain-sensing stations for generating the deformed shapes of flexible aircraft wing spars. The displacement equations have been successfully validated for accuracy by finite-element analysis. The strain-displacement theory that has been developed could also be applied to calculate the deformed shape of simple and tapered beams, plates, and tapered cantilever wing boxes. The displacement equations and associated strain-sensing system (such as fiber optic sensors) form a powerful tool for in-flight deformation monitoring of flexible wings and tails, such as those often employed on unmanned aerial vehicles. Ultimately, the calculated displacement data can be visually displayed in real time to the ground-based pilot for monitoring the deformed shape of unmanned aerial vehicles during flight.

NOMENCLATURE

A cross-sectional area of uniform cantilever beam, in^2

a mean radius of four-ply composite tube wall and aluminum tube wall, or mean radius of Helios 31-ply reinforced spar cap wall, in.

c depth factor of beam (distance between neutral axis to bottom surface of beam), in.

deg   degree

E Young's modulus, lb/in^2

E_L Young's modulus of lamina in fiber direction, lb/in^2

E_T Young's modulus of lamina in direction transverse to fiber direction, lb/in^2

e finite-element span-wise length, in.

G shear modulus, lb/in^2

G_{LT} shear modulus of lamina, lb/in^2

I moment of inertia of tube cross section, in^4

i identification number for strain-sensing station ($= 0, 1, 2, 3,…, n$)

J polar moment of inertia, in^4

j index

l length of cantilever tube, in.

M moment, in-lb

M_i moment at strain-sensing station, x_i, in-lb

n identification number for the last strain-sensing station, $x_n (= l)$

P applied load, lb

SPAR   Structural Performance And Resizing

T_i twisting moment at distortion-sensing station, x_i, in-lb

t thickness of four-ply composite (or aluminum) wall, in.

$\bar{t}$ thickness of 31-ply composite reinforced wall region, in.

UAV   unmanned aerial vehicle

x, y Cartesian coordinates, in.

x_i i-th strain-sensing station, or its axial coordinate, $x = x_i$, in.

y deflection in y-direction at any point, x, between two adjacent strain-sensing stations, $x_{i-1} \le x \le x_i$, in.

y_i deflection in y-direction at strain-sensing station, x_i, in.

γ_i surface distortion angle (shear strain) at distortion-sensing station, x_i, rad

Δl $= l/n$, distance between two adjacent strain-sensing stations (equally spaced), in.

δ_1, δ_2 displacement at two ends of finite element, in.

ε bending strain at any point, in/in.

ε_i bending strain at strain-sensing station, x_i, due to bending only, in/in.

$\bar{\varepsilon}_i$ true bending strain at strain-sensing station, x_i, due to bending and torsion, in/in.

ε_i^p principal tensile strain at distortion-sensing station, x_i, in the 45-deg helical direction, in/in.

θ beam slope at any point, x, between two adjacent strain-sensing stations, $x_{i-1} \le x \le x_i$, rad or deg

θ_i beam slope at strain-sensing station, x_i, rad or deg

ν Poisson's ratio

ν_{LT} Poisson's ratio of lamina

σ bending stress of outermost fiber, lb/in^2

σ_i^p principal tensile stress at twist-sensing station, x_i, in the 45-deg helical direction, in/in.

$(\tau_{\max})_i$ maximum shear stress at distortion-sensing station, i, lb/in^2

ϕ_i cross-sectional twist angle at strain-sensing station, x_i, rad or deg

$(\ )_{i+}$ outboard side of strain-sensing station, x_i

$(\ )_{i-}$ inboard side of strain-sensing station, x_i

INTRODUCTION

Many unmanned aerial vehicles (UAVs) currently in service today must be ultralightweight and designed with highly flexible structural control surfaces. One such vehicle, the Helios flying wing, has a wingspan of 247 ft. The wingspan of the Helios is longer than the wingspans of the U.S. Air Force C-5 military transport (Lockheed Martin Aeronautics Company, Marietta, Georgia), which is 222 ft, and the Boeing 747 commercial jetliner (Boeing Company, Seattle, Washington), which ranges from 195 to 215 ft, depending on the model. Because of an extremely long wingspan, the wings of vehicles such as the Helios will undergo extra-large deformations into high dihedrals during flight, with wingtip deflections reaching as high as 40 ft. This type of deformed shape is similar to a 72-deg circular arc with a 197-ft radius.

Recently the Helios wing broke up in midair while flying at an altitude of approximately 3000 ft. The primary cause of the mishap is believed to have resulted from undamped pitch oscillations of the highly deformed wing, resulting in the breakup of the wing. To avoid future mishaps, a method must be developed in which the wing deformation can be visually monitored during flight. This way, if the

wingtip deflections approach the design limit, the ground-based pilot could execute timely emergency maneuvers to avoid further deformations.

The major load-carrying main spar of the Helios wing is a carbon fiber composite tube (4-in. radius), which is thicker on the top and bottom (spar caps) to improve bending stiffness. The spar also is wrapped with Nomex® and Kevlar® (both registered trademarks of E.I. duPont de Nemours and Company, Wilmington, Delaware) for additional strength. If multiple strain sensors, such as lightweight fiber optic strain-sensing systems, are installed at discrete sensing stations on a beam-like structure (such as the long-span highly flexible Helios flying wing), the strain sensor data can be used to calculate the deflections and cross-sectional twist angles of the beam-like structure and thereby predict its deformed shape during flight.

This report discusses the development of theoretical displacement equations for uniform cantilever beams subjected to bending, torsion, and combined bending and torsion. The displacement equations are expressed in terms of strains, the output of multiple strain sensors embedded on the wing spar surface, for predicting wing deflections and cross-sectional twist angles during flight. The displacement equations and onboard strain-sensing system could form a powerful tool for in-flight wing deformations monitoring by the ground-based pilot for maintaining safe flights of highly flexible flying wings.

HELIOS UNMANNED AERIAL VEHICLE (UAV) FLEXIBLE STRUCTURE

The Helios prototype (fig. 1) is an ultralightweight, unmanned, solar-powered flying wing aircraft (1,600-lb weight) designed to fly at altitudes up to 100,000 ft. Fourteen electric motors (2 hp each) are required to drive 79-in. diameter composite propellers and other systems. The power required for these motors is generated by high-efficiency solar cells spread over the upper surface of the wing. The cruising speed of the Helios is in the range of 19 to 27 mi/h.

The Helios wing has an 8-ft chord length uniform over the 247-ft wingspan. As discussed previously, the wingspan of the Helios is longer than the wingspans of the U.S. Air Force C-5 military transport (222 ft) and the Boeing 747 commercial jetliner (195–215 ft, depending on the model). The maximum wing loading on the Helios 1,976-ft^2 wing is 0.81 lb/ft^2.

IN–FLIGHT WING SHAPE MONITORING

In-flight wing deformation monitoring of ultralightweight flying wing aircraft such as the Helios is particularly difficult because of weight restrictions and highly flexible nature of the extremely long-span structure. Several methods for in-flight monitoring of wing deflections exist for use on conventional aircraft.

One method is the electro-optical flight deflection measurement system, which is composed of onboard optical receivers and several wing-mounted light-emitting targets (ref. 1). This system provides wing displacement information during flight but is too heavy for lightweight flying wing applications.

Another in-flight deflection measurement method is the use of conventional strain gages to collect local strains for wing deflection information. Numerous strain-sensing stations are required to capture the higher displacement modes of the flexible wings. When multiple strain-sensing stations are used, the weight of the strain gage lead wires alone is too heavy and impractical for most weight-conscious lightweight flying wing aircraft.

Fiber optic sensors offer the most attractive alternative to conventional strain gages. They are lightweight, fine, and flexible filaments (approximately the size of human hairs), and they can be highly multiplexed at desired sensing intervals.

THEORETICAL APPROACH

If multiple strain sensors are installed at discrete sensing stations on a cantilever wing spar, sensor data can be used to calculate the deflections and twists of the wing spar during flight. Classical beam theory can be used to develop theoretical slope, deflection, and cross-sectional twist angle equations for the uniform cantilever beam. These displacement equations are written in terms of the strains for calculating the deformed shape of the beam. In the present report, the input strains are calculated from the displacement output of finite-element stress analysis. The accuracy of the newly developed displacement equations (for bending and torsion) for the uniform cantilever beam is then verified by the finite-element displacement output. With slight modifications, the displacement equations developed for the uniform cantilever beam could be applied to predict the deformed shape of simple beams (two-point supported), tapered beams, plates, and tapered cantilever wing boxes.

UNIFORM CANTILEVER BEAMS

In this section, basic displacement equations are developed for a uniform cantilever beam (for example, the tubular spar of the Helios wing) subjected to bending, torsion, and combined bending and torsion. Although the highly flexible wing of the Helios is capable of undergoing extraordinarily large deformations (wingtip deflections up to 40 ft), the local strains on the wing spar surface remain small. Therefore, the classical small strain theory can be used to derive the slope and displacement equations for the uniform cantilever beam.

Bending

In this section, displacement equations for bending only are developed. These equations are used to describe the local slopes and deflections at points along the strain-sensing line on the bottom surface of a uniform cantilever beam of arbitrary cross-sectional shape (for example, circular tubes of the Helios spar).

Moment-Strain Relationship

The classical bending equation for the uniform beam is given by (refs. 2, 3)

$$\frac{d^2 y}{dx^2} = \frac{M(x)}{EI} \tag{1}$$

in which y is the vertical displacement, x is the span-wise coordinate, $M(x)$ is the bending moment, E is the Young's modulus, and I is the moment of inertia.

4

The bending moment, $M(x)$, in equation (1) may be related to the associated bending strain, $\varepsilon(x)$, at the bottom or top fiber (for example, generatrix of the Helios spar tube) through the outermost fiber bending stress equation, $\sigma(x) = [M(x)c]/I$ (refs. 2, 3):

$$\varepsilon(x) = \frac{\sigma(x)}{E} = \frac{M(x)c}{EI} \quad ; \quad \sigma(x) = \frac{M(x)c}{I} \qquad (2)$$

In equation (2), c is the depth factor of the beam (distance between the neutral axis and the bottom surface of the beam). In light of equation (2), the beam bending equation (1) can be written in term of $\varepsilon(x)$ as

$$\frac{d^2 y}{dx^2} = \frac{\varepsilon(x)}{c} \qquad (3)$$

Note that under the strain formulation, beam bending equation (3) contains only the beam geometrical parameter, depth factor, c, and that the flexural rigidity term, EI, is eliminated.

Consider the case of a highly flexible, extremely long tubular spar of the Helios wing that carries concentrated weight (solar-powered motors, pods, hydrogen storage tanks, and so forth) at different wing stations. Because the wing is subjected to aerodynamic lift forces during flight, the wing spar tube bending moment, $M(x)$, could be a complicated nonlinear function of the span-wise coordinate, x.

Strain-Sensing Stations

Figure 2 shows the uniform cantilever tubular spar with a length of l and an outer radius of c. The beam is installed with $n + 1$ equally spaced bending strain sensors at the sensing station, x_i ($i = 0, 1, 2, 3, \ldots, n$), along the bottom or top generatrix, which is a straight line on the tubular surface parallel to the axis, x, of the tubular spar. The first and final strain-sensing stations $\{ x_0(x=0), x_n(x=l) \}$ are located at the built-in end and the beam tip, respectively. The beam is now discretized into n sections with equal length, $\Delta l = l/n$. Although the bending strain is zero at the spar tip, the nth bending strain sensor is installed there because of mathematical convenience in the derivation of the displacement equations.

The bending moment, $M(x)$, can be assumed to be a piecewise-linear function along the axial coordinate, x. Namely, in the region, $x_{i-1} < x < x_i$, between any two adjacent strain-sensing stations, $\{ x_{i-1}, x_i \}$, $M(x)$ is considered as a linear function of $(x - x_{i-1})$ as

$$M(x) = M_{i-1} - (M_{i-1} - M_i)\frac{x - x_{i-1}}{\Delta l} \quad ; \quad x_{i-1} \leq x \leq x_i \qquad (4)$$

in which $\{M_{i-1}, M_i\}$ are the bending moments at the two adjacent strain-sensing stations, $\{x_{i-1}, x_i\}$, respectively, and $\Delta l (= x_i - x_{i-1} = l/n)$ is the axial distance between the two adjacent strain-sensing stations, $\{x_{i-1}, x_i\}$.

In light of equation (2), local moment equation (4) can be written in terms of the local bending strain, $\varepsilon(x)$, for the region, $x_{i-1} < x < x_i$, as

$$\varepsilon(x) = \varepsilon_{i-1} - (\varepsilon_{i-1} - \varepsilon_i)\frac{x - x_{i-1}}{\Delta l} \quad ; \quad x_{i-1} < x < x_i \quad ; \quad \Delta l = \frac{l}{n} \tag{5}$$

in which $\{\varepsilon_{i-1}, \varepsilon_i\}$ are the bending strains measured at the two adjacent sensing stations, $\{x_{i-1}, x_i\}$, respectively.

Slope Equations

The slope, $\tan\theta(x)$, of the uniform beam in the region, $x_{i-1} \leq x \leq x_i$, between the two adjacent strain-sensing stations, $\{x_{i-1}, x_i\}$, can be obtained by integrating equation (3), with the constant of integration determined by enforcing the continuity of the slope at the adjacent inboard strain-sensing station, x_{i-1}, as

$$\tan\theta(x) = \underbrace{\int_{x_{i-1}}^{x}\frac{d^2y}{dx^2}dx}_{\text{Slope increment}} + \underbrace{\tan\theta_{i-1}}_{\text{Slope at } x_{i-1}} = \int_{x_{i-1}}^{x}\frac{\varepsilon(x)}{c}dx + \tan\theta_{i-1} \quad ; \quad x_{i-1} \leq x \leq x_i \tag{6}$$

in which $\tan\theta_{i-1}$ (constant of integration) is the slope at the adjacent inboard strain-sensing station, x_{i-1}. Substituting strain equation (5) into slope equation (6), and carrying out the integration, one obtains the slope, $\tan\theta_i \equiv [\tan\theta(x_i)]$, at the strain-sensing station, x_i, as (ref. 4)

$$\tan\theta_i = \frac{\Delta l}{2c}(\varepsilon_{i-1} + \varepsilon_i) + \tan\theta_{i-1} \quad ; \quad (i = 1, 2, 3, ..., n) \tag{7}$$

Equation (7) is a recursion formula showing that the slope, $\tan\theta_i$, at the strain-sensing station, x_i, is related to the slope, $\tan\theta_{i-1}$, at the adjacent inboard strain-sensing station, x_{i-1}. Applying the descending indices relationship causes slope equation (7) to become

$$\tan\theta_i = \frac{\Delta l}{2c}\left[\varepsilon_0 + 2\sum_{j=1}^{i-1}\varepsilon_j + \varepsilon_i\right] \quad ; \quad (i = 1, 2, 3, ..., n) \tag{8}$$

Note that the slope, $\tan\theta_i$, is determined from the geometrical and strain data evaluated at all the inboard and current strain-sensing stations, ($x_0, x_1, x_2, ..., x_i$). The first objective is to calculate $\tan\theta_i$ (i = 1, 2, 3, ..., n) for all strain-sensing stations. If the last strain-sensing station, x_n, is located at the wingtip, then the slope, $\tan\theta_n$, becomes the wingtip slope.

Deflection Equations

The deflection, $y(x)$, of the uniform beam in the region, $x_{i-1} \leq x \leq x_i$, between the two adjacent strain-sensing stations, $\{x_{i-1}, x_i\}$, can be obtained by integrating slope equation (6) with the constant of

6

integration determined by enforcing the continuity of deflection at the adjacent inboard strain-sensing station, x_{i-1}, as

$$y(x) = \underbrace{\int_{x_{i-1}}^{x} \tan\theta(x)\,dx}_{\text{Integration of slope}} + \underbrace{y_{i-1}}_{\substack{\text{Deflection} \\ \text{at } x_{i-1}}} = \underbrace{\int_{x_{i-1}}^{x}\int_{x_{i-1}}^{x} \frac{\varepsilon(x)}{c}\,dx\,dx}_{\text{Deflection increment}} + \underbrace{\int_{x_{i-1}}^{x} \tan\theta_{i-1}\,dx}_{\substack{\text{Deflection at } x \\ \text{due to } \tan\theta_{i-1}}} + \underbrace{y_{i-1}}_{\substack{\text{Deflection} \\ \text{at } x_{i-1}}} \tag{9}$$

$$x_{i-1} \le x \le x_i$$

in which y_{i-1} (integration constant) is the deflection at the adjacent inboard strain-sensing station, x_{i-1}. Carrying out the integration of equation (9) in light of strain equation (5), one obtains the deflection, $y_i \equiv [y(x_i)]$, at the strain-sensing station, x_i, as (ref. 4)

$$y_i = \frac{(\varDelta l)^2}{6c}\left(2\varepsilon_{i-1} + \varepsilon_i\right) + y_{i-1} + \varDelta l \tan\theta_{i-1} \quad ; \quad (i = 1, 2, 3,..., n) \tag{10}$$

Deflection equation (10) is also a recursion formula showing that the deflection, y_i, at the strain-sensing station, x_i, is expressed in terms of the deflection, y_{i-1}, and the slope, $\tan\theta_{i-1}$, at the adjacent inboard strain-sensing station, x_{i-1}. Applying the descending recursion relationship for y_{i-1} in light of equation (10), and applying expression (8) for $\tan\theta_{i-1}$, one could express deflection equation (10) for y_i as a summation of all the inboard strains including the strain at the current sensing station, x_i:

$$y_i = \frac{(\varDelta l)^2}{6c}\left[(3i-1)\varepsilon_0 + 6\sum_{j=1}^{i-1}(i-j)\varepsilon_j + \varepsilon_i\right] \quad ; \quad (i = 1, 2, 3,..., n) \tag{11}$$

By plotting the deflections, y_i $(i = 1, 2, 3,..., n)$, at the strain-sensing stations, x_i, one can construct the deformed shape of the tubular wing spar, which could be displayed on the screen so that the ground-based pilot can view the real-time wing deformation status.

The contribution of deflection caused by shear effect usually is very small for a long cantilever beam. If shear effect is desired, however, an additional shear effect term must be added to equation (11) (see Appendix B of reference 5).

Torsion

In this section, displacement equations are developed for a tubular cantilever spar under torsion. Consider a cantilever tubular spar of length l, with n number of equally spaced distortion-sensing stations (fig. 2), subjected to span-wise varying twisting moments.

Torque-Twist Relationship

Let T_i be the twisting moment at the distortion-sensing station, x_i, and let γ_i be the associated surface distortion angle (shear strain) at the distortion-sensing station, x_i (fig. 3). The classical torque-distortion
relationship can then be written as (refs.1, 2)

$$\gamma_i = \frac{T_i c}{GJ} \tag{12}$$

in which G is the shear modulus, J is the polar moment of inertia, and c is the outer radius of the wing spar. The surface distortion angle, γ_i (shear strain), in equation (12) is obtained from the distortion sensor output using

$$\gamma_i = \frac{(\tau_{\max})_i}{G} = \frac{\sigma_i^p}{G} = \frac{E}{G}\varepsilon_i^p = 2(1+v)\varepsilon_i^p \tag{13}$$

in which $(\tau_{\max})_i$ is the maximum shear stress at the distortion-sensing station, i, and σ_i^P $[=(\tau_{\max})_i]$ and ε_i^P are the principal tensile stress and strain, respectively, in the 45-deg helical direction at the distortion-sensing station, i (fig. 3).

Cross-Sectional Twists

The total cross-sectional twist angle, ϕ_i, at the strain-sensing station, x_i, can be obtained by summing up all surface distortion angles, γ_j, at all the inboard strain-sensing stations, j (= 1, 2, 3,…, $i-1$), as (fig. 3)

$$\phi_i = \frac{\Delta l}{c}(\gamma_0 + \gamma_1 + \gamma_2 + \gamma_3 + ...+ \gamma_{i-1}) \tag{14}$$

Notice that when equation (14) is written for the beam tip ($i = n$), the resulting expression of the beam tip cross-sectional twist angle, ϕ_n, does not contain the tip distortion term, γ_n. Therefore, installation of the tip distortion sensor for measuring γ_n is not required (fig. 2).

Combined Bending and Torsion

In this section, displacement equations are developed for a cantilever tubular spar under combined bending and torsion. The calculations of true bending strains are presented, from which modified slope and deflection equations are established.

True Bending Strain

As shown in figure 3, if the tubular spar is subjected to torsion in addition to bending, the bending strain-sensing station, x_i (for measuring bending strain, ε_i), will move tangentially by a cross-sectional twist angle, ϕ_i, and the bending strain-sensing axis will be tilted by a local surface distortion angle, γ_i. Thus, the strain output, ε_i, obtained at the sensing station, x_i, no longer gives the true bending strain. To

8

obtain the true bending strain, $\bar{\varepsilon}_i$, the value of the measured strain, ε_i, must be corrected by using the bending strain correction equation,

$$\bar{\varepsilon}_i = \frac{\varepsilon_i}{\cos\phi_i \cos\gamma_i} \tag{15}$$

in which the surface distortion angle, γ_i, and the cross-sectional twist angle, ϕ_i, are calculated from equations (13) and (14), respectively.

Modified Slope and Deflection Equations

With the effect of torsion, slope equation (8) and deflection equation (11) for the bending case must be modified by replacing ε_i with $\bar{\varepsilon}_i$:

$$\tan\theta_i = \frac{\Delta l}{2c}\left[\bar{\varepsilon}_0 + 2\sum_{j=1}^{i-1}\bar{\varepsilon}_j + \bar{\varepsilon}_i\right] \tag{16}$$

$$y_i = \frac{(\Delta l)^2}{6c}\left[(3i-1)\bar{\varepsilon}_0 + 6\sum_{j=1}^{i-1}(i-j)\bar{\varepsilon}_j + \bar{\varepsilon}_i\right] \tag{17}$$

When the true bending strain data, $\{\bar{\varepsilon}_0, \bar{\varepsilon}_1, \bar{\varepsilon}_2, \bar{\varepsilon}_3, ..., \bar{\varepsilon}_i\}$, are substituted, the slopes and deflections of the tubular spar at the strain-sensing stations can be calculated from equations (16) and equations (17), respectively, for the combined bending and torsion loading case.

FINITE–ELEMENT ANALYSIS

To test the prediction accuracy of deflection equation (11), strain sensor data and measured deflection data are needed. Before the experimental data are available, an alternative approach is to use finite-element analysis to generate the desired bending strain and deflection data. The Structural Performance And Resizing (SPAR) finite-element computer program (ref. 6) was used for this purpose. The following section describes the method for generating the bending strains, ε_i, from the SPAR output.

Generation of Bending Strains

From the SPAR nodal displacement output, the axial displacements, $\{\delta_1, \delta_2\}$, at the two ends of the element lying in the lower outermost surface can be used to calculate the bending strain for that particular

element. If the strain-sensing station, x_i, is located in the middle of the element, the displacement differential, $(\delta_2 - \delta_1)$, can be divided by the element axial length, e, to generate the desired bending strain, ε_i, at the sensing cross section, x_i. Namely,

$$\varepsilon_i = \left(\frac{\delta_2 - \delta_1}{e}\right)_i \tag{18}$$

If the sensing station, x_i, is located at the juncture of two adjacent elements, then the following average strain value is used for the strain, ε_i, at the sensing station, x_i:

$$\varepsilon_i = \frac{1}{2}\left[\left(\frac{\delta_2 - \delta_1}{e}\right)_{i+} + \left(\frac{\delta_2 - \delta_1}{e}\right)_{i-}\right] \tag{19}$$

In equation (19), $\{\,()_{i+},\ ()_{i-}\,\}$ denote the elements on the outboard and inboard sides, respectively, of the strain-sensing cross section, x_i.

The SPAR bending strains calculated from equations (18) and (19) can be input to deflection equation (11) to calculate the beam deflections. These calculated deflections can then be compared with the deflections obtained from the SPAR displacement output to check the prediction accuracy of deflection equation (11).

Cantilever Tube Models

Figure 4 shows a typical finite-element model for a cantilever tube with a length of l =100.5 in. The model consists of 100 four-node shell elements in the axial direction and 36 in the circumferential direction. The end disk was added so that the tip load can be applied at the disk center. The cantilever tube is fixed in space at the left end and is subjected to an upward vertical load of P = 100 lb at the tip. The following three types of tubes, fabricated with different materials, were considered:

1. Aluminum tube
2. Four-ply composite tube: carbon fiber composite wall
3. Helios composite tube: carbon fiber composite wall with additional carbon fiber composite reinforcements on the top and bottom of the spar caps.

Table 1 lists the dimensions and table 2 lists the material properties of these three types of tubes.

Table 1. Dimensions of three types of tubular spars.

Tube type	l, in.	a, in.	c, in.	t, in.
Aluminum	100.5	4.0	4.01148	0.02296
Four-ply composite	100.5	4.0	4.01148	0.02296
Helios composite	100.5	4.0* (4.07749)**	4.16646**	0.02296* (0.17794)**

* Four-ply regions   ** Reinforced regions

Table 2. Material properties of carbon fiber composite and aluminum tubes.

Carbon fiber composite	Aluminum
$E_L = 16.3 \times 10^6\, \text{lb/in}^2$	$E = 10.5 \times 10^6\, \text{lb/in}^2$
$E_T = 0.98 \times 10^6\, \text{lb/in}^2$	NA
$G_{LT} = 0.71\, \text{lb/in}^2$	$G = 4.0 \times 10^6\, \text{lb/in}^2$
$v_{LT} = 0.34$	$v = 0.33$

NUMERICAL EXAMPLES – CANTILEVER TUBES

The SPAR displacement output and strain equations (18) and (19) were used to calculate the bending strain, ε_i, for the sensing stations in all cases. These strain values were then input to the appropriate deflection equations to calculate the deflections at all the strain-sensing stations of all the beam cases. This section presents examples of three types of cantilever tubes (aluminum, four-ply composite, and Helios composite). The deflections calculated from the Ko displacement theories are compared with those calculated from the SPAR finite-element analysis.

Aluminum Cantilever Tube

Figure 5 shows the bending strains, ε_i, at the sensing stations on the aluminum tube, calculated from the SPAR nodal displacement output. The strain data from figure 5 were used to calculate the deflections, y_i, from deflection equation (11). Table 3 compares the deflections, y_i, calculated from deflection equation (11) with those obtained from the SPAR displacement output for the case of $n = 8$ ($n+1 = 9$ strain-sensing stations). Note that the difference between the deflection values calculated from the SPAR program and those calculated from equation (11) is minimal for the present uniform cantilever aluminum tube.

Table 3. Comparison of deflections calculated from SPAR with those calculated from deflection equation (11); aluminum cantilever tube; $n = 8$.

	Deflection (y_i), in.								
	y_0	y_1	y_2	y_3	y_4	y_5	y_6	y_7	y_8
SPAR	0.0000	0.0179	0.0636	0.1341	0.2253	0.3330	0.4530	0.5814	0.7138
Deflection equation (11)	0.0000	0.0157	0.0605	0.1302	0.2205	0.3273	0.4465	0.5738	0.7051
Difference, percent	0.0000	12.2142	4.9356	2.9223	2.1262	1.7208	1.4524	1.3072	1.2230

The data in table 3 are plotted in figure 6. The two sets of deflection curves are quite close, indicating the accuracy of deflection equation (11). The deflection curves calculated from equation (11) lie slightly below those obtained from the SPAR output.

Four-Ply Composite Cantilever Tube

Figure 7 shows the bending strain curve, ε_i, calculated from the SPAR output, for the strain-sensing stations on the four-ply composite tube. In this case the SPAR strain curve is practically linear. The strain data from figure 7 were used to calculate the deflections, y_i, from deflection equation (11) for the case of $n = 8$. Table 4 compares the deflections, y_i, calculated from deflection equation (11) with those obtained from the SPAR displacement output. Again, the difference between the values calculated from the SPAR program and those calculated from equation (11) is minimal.

Table 4. Comparison of deflections calculated from SPAR with those calculated from deflection equation (11);   four-ply composite cantilever tube; $n = 8$.

	Deflection (y_i), in.								
	y_0	y_1	y_2	y_3	y_4	y_5	y_6	y_7	y_8
SPAR	0.0000	0.0749	0.2577	0.5421	0.9110	1.3475	1.8347	2.3558	2.8946
Deflection equation (11)	0.0000	0.0658	0.2519	0.5413	0.9167	1.3610	1.8570	2.3877	2.9356
Difference, percent	0.0000	12.2264	2.2545	0.1531	0.6301	1.0000	1.2176	1.3526	1.4154

The data from table 4 are plotted in figure 8 for visual comparison. The two deflection curves are quite close, indicating the accuracy of deflection equation (11). The deflection curves calculated from deflection equation (11) for the four-ply composite tube lie slightly above those obtained from the SPAR output.

Helios Composite Cantilever Tube

Figure 9 shows the bending strain curve, ε_i, calculated from the SPAR output, for the strain-sensing stations on the Helios composite tube. In this case, the SPAR strain curve is nearly linear. The strain data from figure 9 were used to calculate the deflections, y_i, from deflection equation (11) for the case of $n = 8$. Table 5 compares the deflections, y_i, calculated from deflection equation (11) with those obtained from the SPAR displacement output. Again, the difference between the beam-tip displacement values calculated from the SPAR program and those calculated from deflection equation (11) is minimal.

Table 5. Comparison of deflections calculated from SPAR with those calculated from deflection equation (11); Helios composite cantilever tube; $n = 8$.

	Deflection (y_i), in.								
	y_0	y_1	y_2	y_3	y_4	y_5	y_6	y_7	y_8
SPAR	0.0000	0.0240	0.0673	0.1324	0.2167	0.3166	0.4284	0.5479	0.6721
Deflection equation (11)	0.0000	0.0152	0.0577	0.1235	0.2089	0.3099	0.4227	0.5432	0.6676
Difference, percent	0.0000	36.7126	14.2263	6.6853	3.5818	2.1381	1.3307	0.8669	0.6725

The data from table 5 are plotted in figure 10 for visual comparison. The two deflection curves are quite close, indicating the accuracy of deflection equation (11). The deflection curves calculated from deflection equation (11) for the Helios composite tube lie slightly below those obtained from the SPAR output.

DISCUSSION

In-flight predictions of the deformed shape of the ultralightweight flying wing require the installation of multiple bending and distortion strain sensors, equally spaced on the surface of the tubular wing spar, for measuring the bending and distortion strains of the wings. The strain sensor data can then be input to theoretical displacement equations for calculating slopes, deflections, and twist angles of the wing spar at all strain-sensing stations, including the sensing station on the spar tip.

Because the accuracy of the displacement (bending and torsion) equations has been validated by finite-element analysis, the equations are ready for application. To solidify confidence, however, the accuracy of the equations must be checked extensively by testing several types of continuous and composite cantilever tubular beams under bending, torsion, and combined bending and torsion. The validation experiments are currently under way.

When strain sensors are installed on the wing spar (or wing box), the displacement equations together with strain sensor data can be used to construct the in-flight deformed shape of an aircraft such as the Helios flying wing. Because they are lightweight, fiber optic sensors may be the optimal choice for the embedded strain sensors on the wing spar surface. The use of a conventional strain gage sensing system is impractical, because it has numerous lead wires that add weight, thus it is too heavy for the lightweight flying wing to carry.

The displacement theory that has been developed can also be applied to calculate the deformed shape of simple beams and plates (ref. 5). The displacement theories can be extended to cases of nonuniform beams, such as tapered cantilever wing boxes and aircraft fuselages (varying cross sections) under combined bending and torsion (ref. 5).

CONCLUDING REMARKS

Displacement equations were developed for a cantilever tubular wing spar under bending, torsion, and combined bending and torsion loading. These displacement equations were expressed in terms of strains

measured at multiple sensing stations equally spaced on the surface of the wing spar. The principal results are as follows:

1. The displacement equations developed for the uniform cantilever beam were successfully validated for accuracy by classical beam theory and finite-element analysis.

2. The deflections predicted from the deflection equations for the three types of cantilever tubular spars
agreed quite well with the deflections calculated from the finite-element analysis.

3. The deflection equations and associated strain-sensing system (such as fiber optic sensors) form a powerful tool for in-flight calculations of slopes, deflections, and cross-sectional twist angles of the wing spar at any strain-sensing station. These calculated displacements can be used to construct the deformed shape of the long-span flying wing. Ultimately, the calculated deformation data can be visually displayed in real time for the ground-based pilot to monitor the in-flight deformed shape of unmanned aerial vehicles.

FIGURES

Figure 1. Solar powered Helios prototype flying wing during a test flight over the Pacific Ocean.

$$M(x) = M_{i-1} - \left(M_{i-1} - M_i\right)\frac{x - x_{i-1}}{\Delta l} \; ; \; x_{i-1} < x < x_i$$
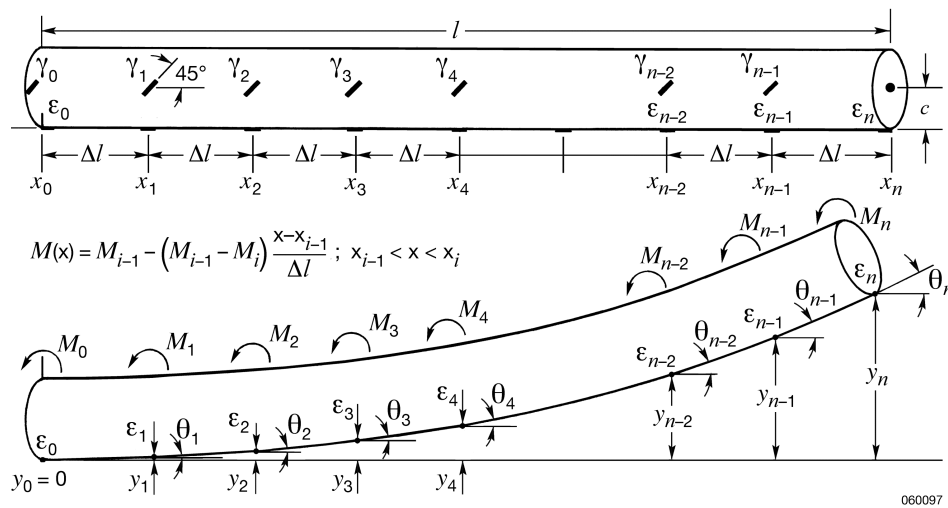
Figure 2. Cantilever tubular spar with equally spaced bending and torsion strain sensors.
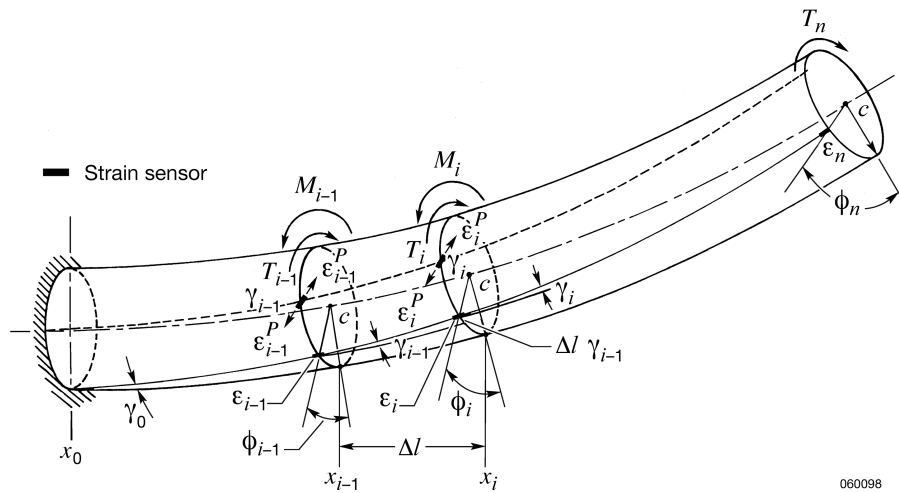
Figure 3. Instrumented cantilever tubular spar under combined bending and torsion.
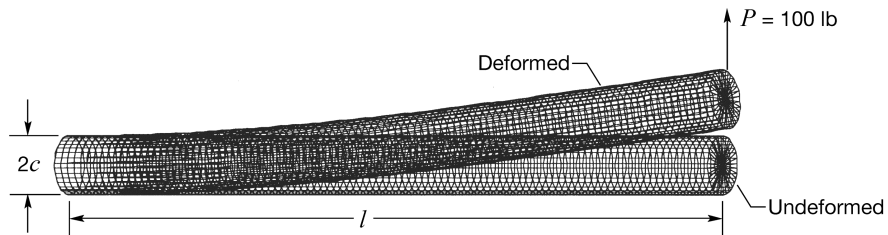
l = 100.5 in.
a = 4 in.   (Al, four-ply walls)
t = 0.02296 in. (Al, four-ply walls)
a = 4.07749 in. (Helios spar caps)
$\bar{t}$ = 0.17784 in. (Helios spar caps)
c = a + 0.5t

Nodes	3673
Four-node elements	3636
Three-node elements	36

Figure 4. Helios tubular spar finite-element model subjected to a vertical tip load of P = 100 lb.
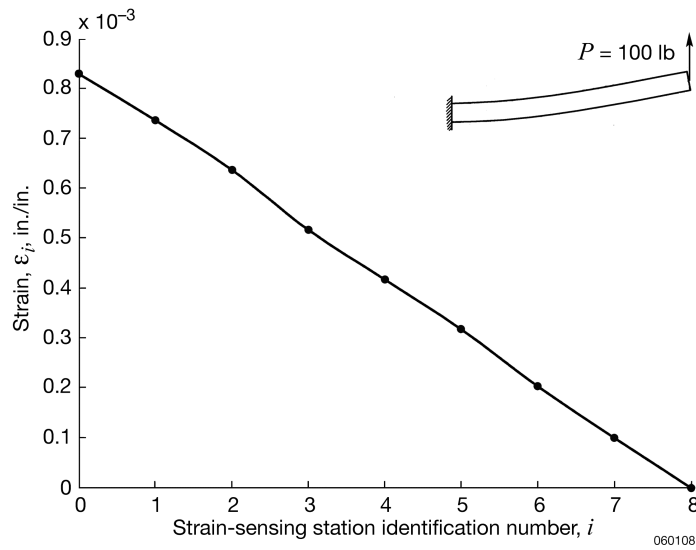
Figure 5. Bending strains, ε_i, at different sensing stations, x_i, calculated from the SPAR program; aluminum cantilever tube; $n = 8$; P = 100 lb.
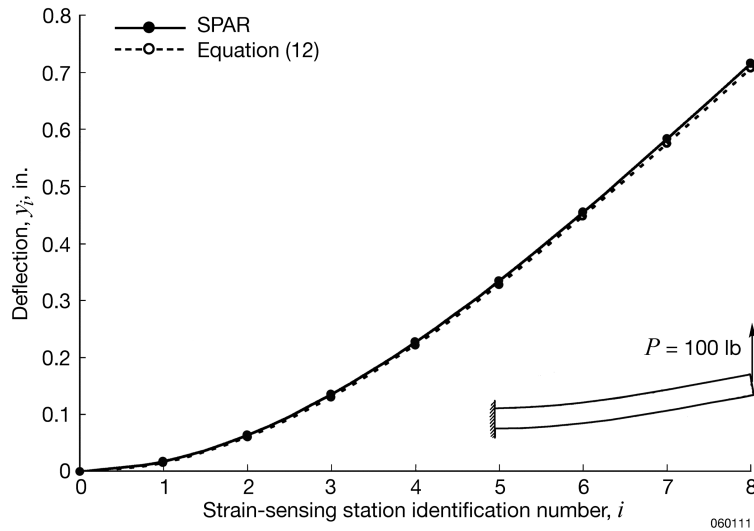
Figure 6. Comparison of deflections calculated from SPAR with those calculated from deflection equation (11); aluminum cantilever tube; $n = 8$; P = 100 lb.
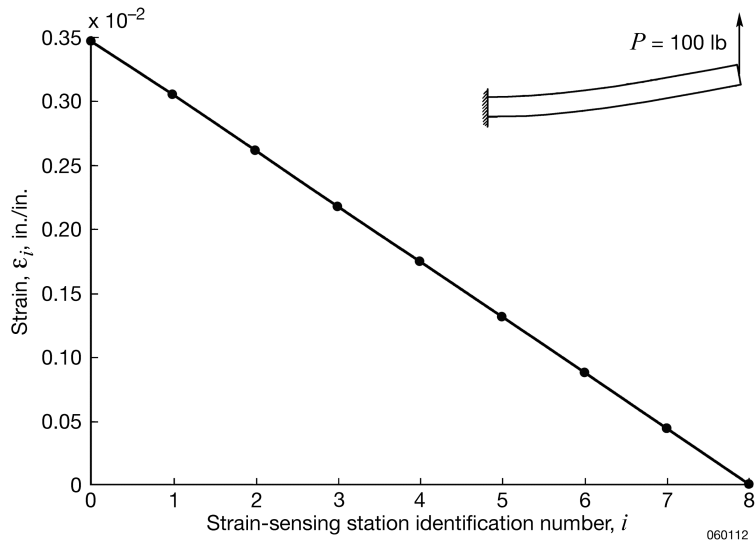
Figure 7. Bending strains, ε_i, at different sensing stations, x_i, calculated from the SPAR program; four-ply composite cantilever tube; $n = 8$; P = 100 lb.
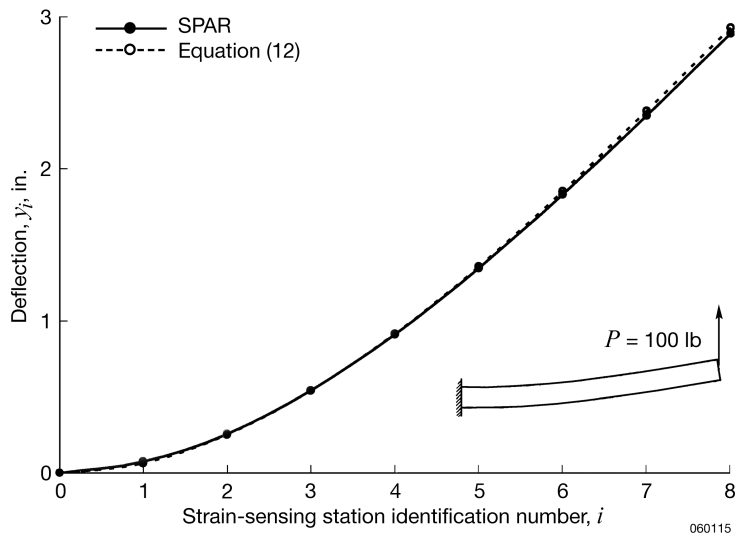
Figure 8. Comparison of deflections calculated from SPAR with those calculated from deflection equation (11); four-ply composite cantilever tube; $n = 8$; P = 100 lb.
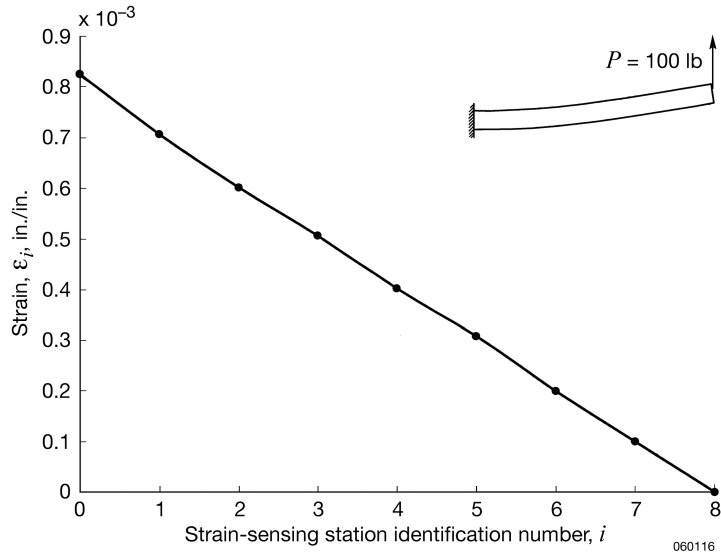
Figure 9. Bending strains, ε_i, at different sensing stations, x_i, calculated from the SPAR program; Helios composite cantilever tube; $n = 8$; P = 100 lb.
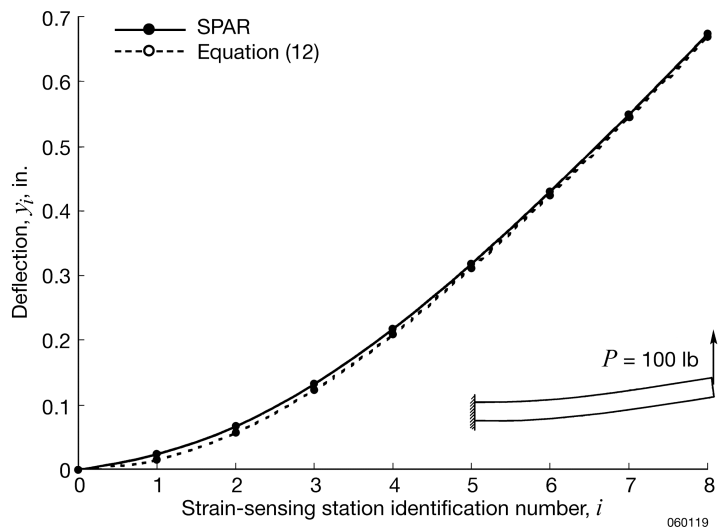
Figure 10. Comparison of deflections calculated from SPAR with those calculated from deflection equation (11); Helios composite cantilever tube; $n = 8$; P = 100 lb.

REFERENCES

1. DeAngelis, V. Michael, and Robert Fodale, "Electro-Optical Flight Deflection Measurement System," *Society of Flight Test Engineers 18th Annual Symposium*, Paper No. 22, Amsterdam, Netherlands, Sept. 1987.

2. Roark, Raymond J., *Formulas for Stress and Strain*, Third Edition, McGraw-Hill Book Company, Inc., New York, 1954.

3. Faupel, Joseph H., *Engineering Design: A Synthesis of Stress Analysis and Materials Engineering*, John Wiley and Sons, Inc., New York, 1964.

4. Hodgman, Charles D., *Standard Mathematical Tables*, Seventh Edition, Chemical Rubber Publishing Company, Cleveland, 1957.

5. Ko, William L., W.L. Richards, and Van T. Tran, *Displacement Theories for In-Flight Deformed Shape Predictions of Aerospace Structures*, NASA/TP-2007-214612, 2007.

6. Whetstone, W.D., *SPAR Structural Analysis System Reference Manual*, System Level 13A, Vol. 1, Program Execution, NASA CR-158970-1, 1978.

1. REPORT DATE (DD-MM-YYYY)	2. REPORT TYPE	3. DATES COVERED (From - To)
01-08-2010	Technical Publication	

4. TITLE AND SUBTITLE	5a. CONTRACT NUMBER
Methods for In-Flight Wing Shape Predictions of Highly Flexible Unmanned Aerial Vehicles: Formulation of Ko Displacement Theory	
	5b. GRANT NUMBER
	5c. PROGRAM ELEMENT NUMBER
6. AUTHOR(S)	5d. PROJECT NUMBER
Ko, William L. and Fleischer, Van Tran	
	5e. TASK NUMBER
	5f. WORK UNIT NUMBER

7. PERFORMING ORGANIZATION NAME(S) AND ADDRESS(ES)	8. PERFORMING ORGANIZATION REPORT NUMBER
NASA Dryden Edwards, Ca 93523-0273	H-3044

9. SPONSORING/MONITORING AGENCY NAME(S) AND ADDRESS(ES)	10. SPONSORING/MONITOR'S ACRONYM(S)
National Aeronautics and Space Administration Washington, DC 20546-0001	NASA
	11. SPONSORING/MONITORING REPORT NUMBER
	NASA/TP-2010-214656

12. DISTRIBUTION/AVAILABILITY STATEMENT

Unclassified -- Unlimited
Subject Category 39   Availability: NASA CASI 443-757-5802   Distribution: Standard

13. SUPPLEMENTARY NOTES

Ko and Fleischer, NASA Dryden Flight Research Center

14. ABSTRACT

The Ko displacement theory is formulated for a cantilever tubular wing spar under bending, torsion, and combined bending and torsion loading. The Ko displacement equations are expressed in terms of strains measured at multiple sensing stations equally spaced on the surface of the wing spar. The bending and distortion strain data can then be input to the displacement equations to calculate slopes, deflections, and cross-sectional twist angles of the wing spar at the strain-sensing stations for generating the deformed shapes of flexible aircraft wing spars. The displacement equations have been successfully validated for accuracy by finite-element analysis. The Ko displacement theory that has been formulated could also be applied to calculate the deformed shape of simple and tapered beams, plates, and tapered cantilever wing boxes. The Ko displacement theory and associated strain-sensing system (such as fiber optic sensors) form a powerful tool for in-flight deformation monitoring of flexible wings and tails, such as those often employed on unmanned aerial vehicles. Ultimately, the calculated displacement data can be visually displayed in real time to the ground-based pilot for monitoring the deformed shape of unmanned aerial vehicles during flight.

15. SUBJECT TERMS

Beam curvature equation, Displacement equations, Distributed surface strains, Ko Displacement Theory, Structural shape predictions

16. SECURITY CLASSIFICATION OF:			17. LIMITATION OF ABSTRACT	18. NUMBER OF PAGES	19b. NAME OF RESPONSIBLE PERSON
a. REPORT	b. ABSTRACT	c. THIS PAGE			STI Help Desk at email: help@sti.nasa.gov
					19b. TELEPHONE NUMBER (Include area code)
U	U	U	UU	25	(443) 757-5802